Path integral Monte Carlo simulations of warm dense aluminum

K. P. Driver, François Soubiran, B. Militzer

▶ **To cite this version:**

K. P. Driver, François Soubiran, B. Militzer. Path integral Monte Carlo simulations of warm dense aluminum. Physical Review E , 2018, 97 (6), 10.1103/PhysRevE.97.063207 . hal-02322968

HAL Id: hal-02322968

https://univ-lyon1.hal.science/hal-02322968v1

Submitted on 10 Mar 2022

HAL is a multi-disciplinary open access archive for the deposit and dissemination of scientific research documents, whether they are published or not. The documents may come from teaching and research institutions in France or abroad, or from public or private research centers.

L'archive ouverte pluridisciplinaire **HAL**, est destinée au dépôt et à la diffusion de documents scientifiques de niveau recherche, publiés ou non, émanant des établissements d'enseignement et de recherche français ou étrangers, des laboratoires publics ou privés.

Path integral Monte Carlo simulations of warm dense aluminum

K. P. Driver,[1,*] F. Soubiran,[1,†] and B. Militzer[1,2]
[1]*Department of Earth and Planetary Science, University of California, Berkeley, California 94720, USA*
[2]*Department of Astronomy, University of California, Berkeley, California 94720, USA*

(Received 17 October 2017; revised manuscript received 19 April 2018; published 25 June 2018)

We perform first-principles path integral Monte Carlo (PIMC) and density functional theory molecular dynamics (DFT-MD) calculations to explore warm dense matter states of aluminum. Our equation of state (EOS) simulations cover a wide density-temperature range of 0.1–32.4 g cm^{-3} and 10^4–10^8 K. Since PIMC and DFT-MD accurately treat effects of the atomic shell structure, we find two compression maxima along the principal Hugoniot curve attributed to K-shell and L-shell ionization. The results provide a benchmark for widely used EOS tables, such as SESAME, QEOS, and models based on Thomas-Fermi and average-atom techniques. A subsequent multishock analysis provides a quantitative assessment for how much heating occurs relative to an isentrope in multishock experiments. Finally, we compute heat capacity, pair-correlation functions, the electronic density of states, and $\langle Z \rangle$ to reveal the evolution of the plasma structure and ionization behavior.

DOI: 10.1103/PhysRevE.97.063207

I. INTRODUCTION

The analysis and interpretation of high-energy density states of matter, commonly found in stellar and planetary interiors [1,2] and inertial confinement fusion [3–5] experiments, requires knowledge of thermophysical material properties at extreme conditions. Aluminum, a simple metal, has been one of the most commonly studied prototype materials for gaining insight into physical properties at such conditions. The wide breadth of experimental and theoretical research on aluminum includes studies of solid phase transitions [6,7], shock physics [8–18], x-ray diagnostics for basic plasma physics [19–34], and optical [35–39] and transport [40–47] properties.

In addition to aluminum being a prototype for studying basic plasma physics, laser-induced shock-wave experiments often use aluminum as a shock standard [18] whose mechanical response is assumed to be well represented by equation of state (EOS) tables [48], such as SESAME [49] and QEOS [50–52]. The EOS of aluminum has been the focus of a number of shock experiments [11,13,15,53] and theoretical investigations, including approaches based on Thomas-Fermi [54], semiempirical [55–59], density functional theory molecular dynamics (DFT-MD) [36,40,60–63], average atom [42,64–68], orbital-free DFT (OF-DFT) [63,69], and extended-plane-wave DFT [70] models. There have been some attempts to compare various models [71,72], which find general agreement with available shock measurements. However, the highest-pressure shock data, derived from nuclear tests, tend to have large error bars, and models can differ significantly in the stiffness of the shock Hugoniot curve. Furthermore, models vary substantially in their treatment of shell-ionization effects, with DFT-MD-based methods providing the most rigorous quantum mechanical treatment so far.

In this paper, our focus is on further exploring the accuracy of the equation of state of aluminum in the warm dense matter (WDM) and plasma regimes, particularly where the influence of electronic shell structure becomes important [12]. Because of the relevance of aluminum for WDM physics, it is desirable to have a first-principles EOS that spans the the condensed matter, warm dense matter, and plasma physics regimes as a reference for shock experiments and hydrodynamic simulations. In recent works, we have developed a first-principles framework to compute coherent EOSs across a wide range of density-temperature regimes relevant to WDM by combining results from state-of-the-art path integral Monte Carlo (PIMC) and DFT-MD methods for first [74]- and second-row [75] elements. Here we use PIMC and DFT-MD to compute a benchmark for the EOS of aluminum in the WDM regime. We also study the temperature-density evolution of the plasma structure and ionization throughout the WDM regime. And, finally, we compare our combined PIMC and DFT-MD shock Hugoniot curve with widely used models and experiments.

The paper is organized as follows: Sec. II describes the simulation methods and details. Section III examines the internal energy and pressure EOS. Section IV discusses the shock Hugoniot curves. Section V characterizes the plasma structure evolution and ionization as a function of temperature and density via pair-correlation functions. Section VI analyzes the electronic density of states as a function of density and pressure, and finally Sec. VII summarizes our work.

II. SIMULATION METHODS

Rigorous discussions of the PIMC [76–78] and DFT molecular dynamics (DFT-MD) [79–81] methods have been provided in previous works, and the details of our simulations

*Current address: Lawrence Livermore National Laboratory, Livermore, CA 94550, USA; driver7@llnl.gov; http://militzer.berkeley.edu/
†Current address: Ecole Normale Supérieure de Lyon, Université Claude Bernard Lyon 1, Laboratoire de Géologie de Lyon, CNRS UMR 5276, Lyon, France.

 ©2018 American Physical Society

have been presented in some of our previous publications [74,75,82–93]. Here we summarize the methods and provide the simulation parameters specific to simulations of aluminum plasma.

The general idea of our approach is to perform simulations along isochores at high temperatures ($T \geqslant 2 \times 10^6$ K) using PIMC and at low temperatures ($T \leqslant 2 \times 10^6$ K) using DFT-MD. We show the two methods produce consistent results at overlapping temperatures. The PIMC method samples the space of all quantum paths to determine the thermal density matrix of the many-body system. PIMC increases in efficiency with temperature (scaling as $1/T$) as quantum paths become shorter and more classical in nature. In contrast, DFT-MD becomes increasingly inefficient with increasing temperature, as the number of partially occupied bands increases unfavorably with temperature (scaling roughly as $\sim T^{3/2}$). The only uncontrolled approximation in PIMC is the use of the fixed-node approximation, which restricts paths to avoid the well-known fermion sign problem [94]. The fermion sign problem is a numerical instability due to the Pauli exclusion principle. We have shown the associated error is small for relevant systems at high enough temperatures [74,76,78]. The main approximation in DFT-MD is the use of an approximate exchange-correlation (XC) functional, though at temperatures relevant to WDM, error in the XC is small relative to the total internal energy, which is the most relevant quantity for EOS and Hugoniot simulations [46].

PIMC uses a small number of controlled approximations, whose errors can be minimized by converging parameters, such as the time step and system size. To address the fermion sign problem, we used the restricted path approach with Hartree-Fock nodes [75,90]. The nodes were enforced in imaginary time steps of 1/8192 Ha, while the pair density matrices were evaluated in steps of 1/1024 Ha. This results in using between 1200 and 12 time slices for the temperature range studied with PIMC (2×10^6 to 2.16×10^8 K) and these choices converged the internal energy per atom to better than 1%. Regarding finite size errors, we have shown that simulations of 8- and 24-atom cubic cells provide internal energies that agree within 1.0% and pressures that agree within 0.5% over the relevant temperature range for PIMC ($T > 1 \times 10^6$ K) [85]. Our results for the internal energy and pressure typically have statistical errors of 0.3% or less.

We employ standard Kohn-Sham DFT-MD simulation techniques for our low temperature ($T \leqslant 2 \times 10^6$ K) calculations. The bulk of these simulations are performed with the Vienna *Ab initio* Simulation Package (VASP) [95] using the projector augmented-wave (PAW) method [96,97], and a NVT ensemble, regulated with a Nosé thermostat. Exchange-correlation effects are described using the local density approximation (LDA) [98]. We used a corresponding PAW-LDA pseudopotential, which will be discussed further below. Electronic wave functions are expanded in a plane-wave basis with a energy cutoff as high as 8000 eV in order to converge the total energy. Size convergence tests up to a 64-atom simulation cell at temperatures of 10 000 K and above indicate that internal energies are converged to better than 0.1% and pressures are converged to better than 0.5%. We find, at temperatures above 250 000 K, eight-atom supercell results are sufficient for both energy and pressure since the kinetic energy far outweighs the interaction energy at such high temperatures [85]. The number of bands in each calculation were selected such that orbitals with occupations as low as 10^{-4} were included, which requires up to 15 000 bands in a eight-atom cell at 2×10^6 K and 1-fold compression. All simulations are performed at the Γ-point of the Brillouin zone, which is sufficient for high temperature fluids, converging total energy to better than 0.01% compared to a grid of k-points.

We encountered some convergence difficulties with the VASP 1s-core pseudopotential (cutoff radius of 1.7 Bohr) at high temperatures ($T \geqslant 2.5 \times 10^5$ K) because the number of projectors used to produce the PAW Al pseudopotentials in the standard VASP library are not optimized for the high-energy cutoffs needed for warm dense matter conditions. In order to alleviate this issue, we first performed MD simulations using a larger, 2s-core pseudopotential (cutoff radius of 2.0 Bohr) in order to generate a sensible statistical ensemble. We then recomputed energies of twenty snapshots chosen randomly from the reference ensemble with the smaller, 1s-core pseudopotential, which is necessary for including core-electron excitations at high temperatures and avoiding core overlap at high densities. In order to reweight the snapshot energies according to the reference ensemble, we employ a umbrella sampling technique. Umbrella sampling is a well-known molecular simulation technique [99] in which non-Boltzmann Monte Carlo is used to estimate free energies. We reweight the energies of the 20 snapshots according the reference ensemble as follows:

$$\langle \mathcal{O} \rangle_2 = \frac{\langle \mathcal{O}(\mathbf{R}) \exp -[\beta_2 E_2(\mathbf{R}) - \beta_1 E_1(\mathbf{R})] \rangle_1}{\langle \exp -[\beta_2 E_2(\mathbf{R}) - \beta_1 E_1(\mathbf{R})] \rangle_1}, \quad (1)$$

where $\mathcal{O}$ denotes the thermodynamical quantity whose average we are computing (energy or pressure), the subscripts 1 and 2 denote the ensemble with which the average is associated, E is the energy, and $\beta = 1/(k_B T)$.

In order to further validate our VASP pseudopotential results and the umbrella sampling approach, we sought to verify our results with a more robust pseudopotential specifically designed for high temperature and densities. For this effort, we constructed a new, PAW pseudopotential for the ABINIT package [100], which allows one to build a specific PAW-pseudopotential using the AtomPAW plugin [101]. We built a hard PAW pseudopotential with a cutoff radius of 0.6 Bohr and a frozen 1s core. To ensure the robustness of the pseudopotential at high temperature, we included projectors with energies as high as 330 Ha. We checked the accuracy of the pseudopotential by reproducing cold-curve results provided by the ELK software in the linearized augmented plane wave (LAPW) framework [102]. With this pseudopotential, we performed DFT-MD calculations with ABINIT using 16-atom and eight-atom cells for three densities (4-, 4.5-, and 5-fold of ρ_0), which are most significant for shell-structure effects in subsequent shock Hugoniot curve analysis, and temperatures up to 4×10^6 K. The hardness of the pseudopotential required a plane-wave energy cutoff of at least 6800 eV, which required significantly more computer time than the VASP calculations and made it unrealistic to explore the entire EOS ρ-T regime with such a demanding pseudopotential. ABINIT results for pressure and energy will be compared with VASP and PIMC in Sec. III.

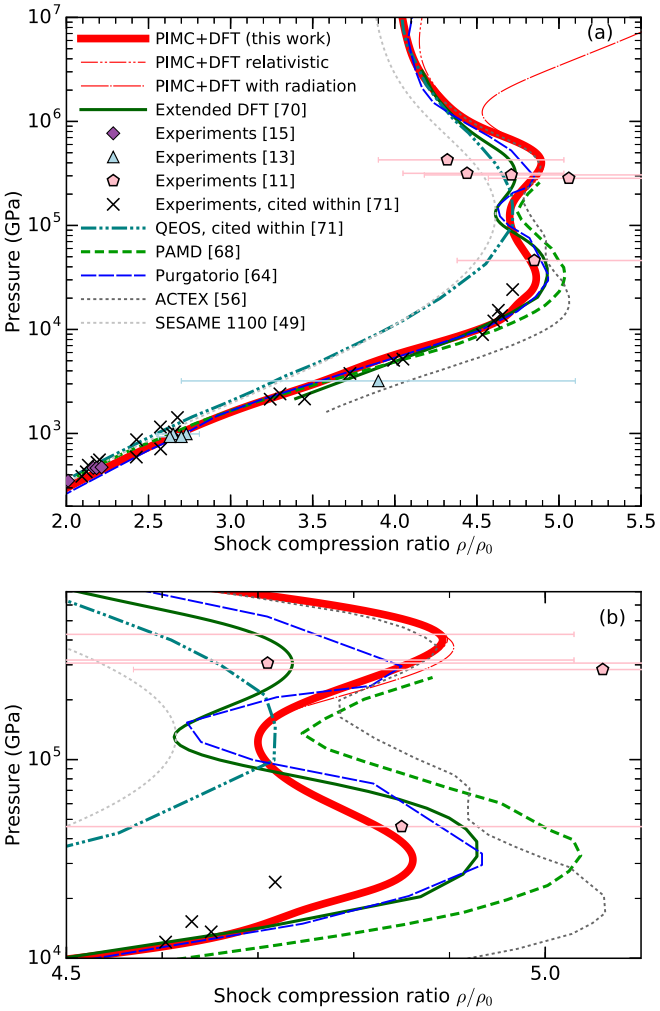

FIG. 1. (a) Comparison of the combined PIMC and DFT-MD principal shock Hugoniot curve (P-ρ/ρ_0 space, $\rho_0 = 2.70$ g cm^{-3}) with experiments [11,13,15,53] and various models, including the QEOS [50,73] and SESAME-1100 [49] tables, Purgatorio [64], ACTEX [56], Pseudoatom MD [68], and extended-plane-wave DFT [70]. Methods that treat the quantum-mechanical shell structure of the ions reveal two compression maxima due to K-shell and L-shell ionization. The QEOS and SESAME tables are derived from models that do not explicitly treat shell effects and, thus, only predict an average ionization behavior. (b) A magnification of the compression maxima.

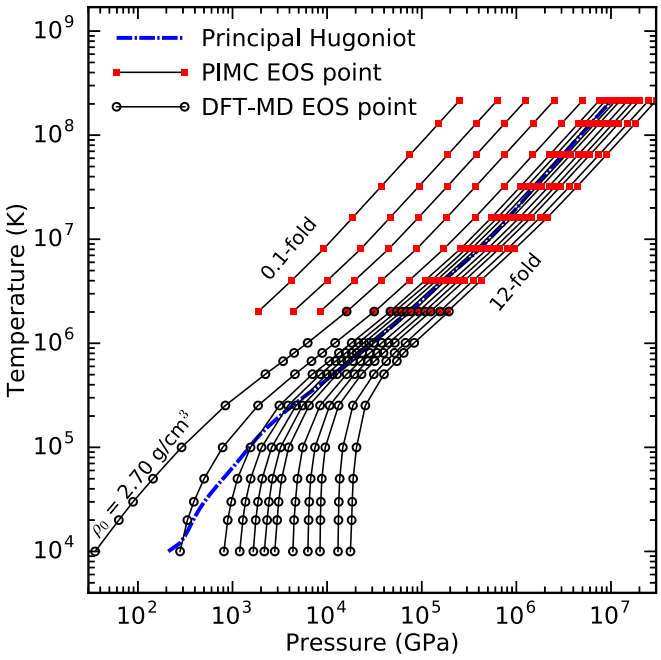

FIG. 2. Temperature-pressure conditions for the PIMC and DFT-MD calculations along isochores corresponding to the densities of 0.1-fold (0.27 g cm^{-3}) to 12-fold (32.38 g cm^{-3}). The blue, dash-dotted line shows the principal Hugoniot curve for an initial density of $\rho_0 = 2.70$ g cm^{-3}.

III. EQUATION OF STATE RESULTS

In this section, we report our combined PIMC and DFT-MD EOS results for the WDM and plasma regimes at several densities in the range of 2.70–32.38 gcm^{-3} and temperatures ranging from 10^4–10^8 K. The full range of our EOS data is shown in pressure-density space in Fig. 1 and in temperature-pressure space in Fig. 2. These two figures will be discussed more thoroughly in Sec. VI. The Supplemental Material [103] provides a table of our full EOS data set. In order to put the PAW-LDA pseudopotential energies on the same scale as all-electron calculations, we shifted all of our VASP DFT-MD energies by −241.30 Ha/atom. The ABINIT pseudopotential shift is −161.33. These shifts were determined by performing isolated, all-electron atomic calculations with the OPIUM code [104] and corresponding calculations in VASP and ABINIT.

In order to analyze the coherence of our EOS data sets, Figs. 3 and 4 display the pressure and internal energy, respectively, along three isochores from PIMC, DFT-MD, and the classical Debye-Hückel plasma model [105] as a function of temperature. The pressures, P, and internal energies, E, are plotted relative to a fully ionized Fermi gas of electrons and ions with pressure, P_0, and internal energy, E_0, in order to compare only the excess pressure and internal energy contributions that result from particle interactions. With increasing temperature, the pressure and internal energy contributions due to interactions gradually decrease from the strongly interacting condensed matter regime, where bound states dominate, to the weakly interacting, fully ionized plasma regime, where PIMC converges to the classical the Debye-Hückel model. As expected, the Debye-Hückel model becomes inadequate for lower, WDM-range temperatures ($T < 10^7$ K) since it fails to treat bound electronic states. While the range of temperatures over which PIMC EOS data are needed to fill the temperature gap between DFT-MD and Debye-Hückel (roughly $2 \times 10^6 - 1 \times 10^7$ K) is relatively small compared to the entire temperature range of the high energy density physics regime, this temperature range encompasses significant portions of the L-shell and K-shell ionization regime.

Figures 3 and 4 provide a coherent EOS over wide density-temperature range, where PIMC and DFT-MD provide consistent results at 2×10^6 K, with differences of 0.5%–3.2% in the pressure and 1%–4% ($\leqslant$5 Ha/Al) in the internal energy. We note the overall agreement between PIMC and DFT-MD provides validation for the use of zero-temperature exchange

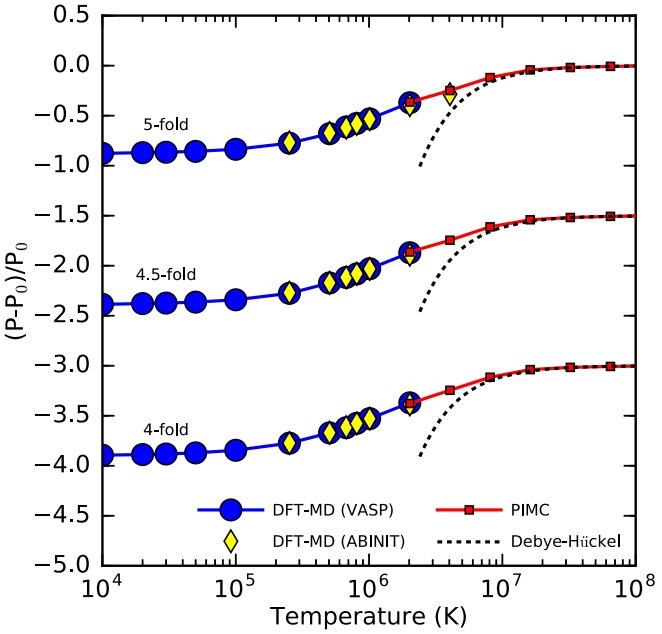

FIG. 3. Aluminum excess pressure, relative to the ideal Fermi gas, computed with PIMC, DFT-MD, and the Debye-Hückel plasma model. The results are plotted at densities corresponding to 4-fold, 4.5-fold, and 5-fold compression as a function of temperature. DFT-MD results using a more robust pseudopotential in ABINIT validate the VASP DFT-MD calculations. The 4- and 4.5-fold curves were shifted vertically for visibility by −3 and −1.5, respectively.

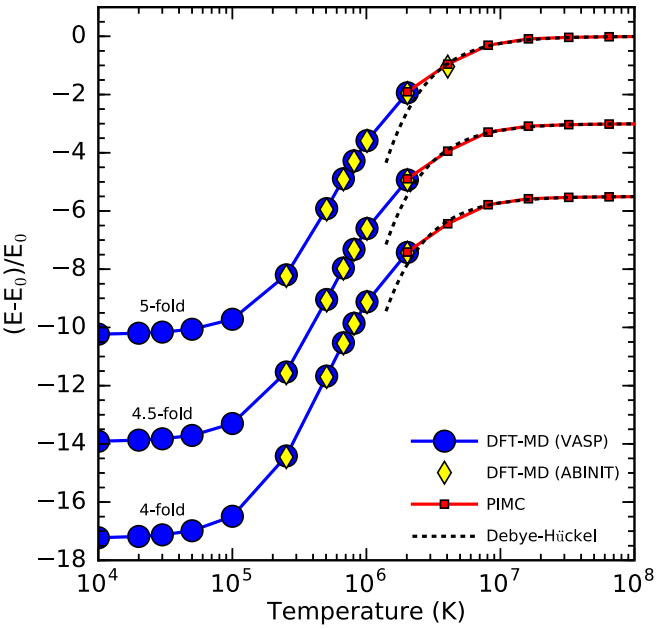

FIG. 4. Aluminum excess internal energy, relative to the ideal Fermi gas, computed with PIMC, DFT-MD, and the Debye-Hückel plasma model. The results are plotted for densities corresponding to 4-fold, 4.5-fold, and 5-fold compression as a function of temperature. DFT-MD results using a more robust pseudopotential in ABINIT validate the VASP DFT-MD calculations. The 4- and 4.5-fold curves were shifted vertically for visibility by −5.5 and −3, respectively.

correlation functionals in WDM applications and the use of the fixed-node approximation in PIMC in the relevant temperature range. At lower temperatures, PIMC results become inconsistent with DFT-MD results because the nodal approximation in PIMC simulations is no longer appropriate. Additionally, we verified the integrity of our calculations in the VASP code by comparing the pressure and internal energy with calculations from the ABINIT DFT-MD code that employ a more robust PAW pseudopotential.

In Fig. 5 we show the heat capacity, c_v, of hot dense aluminum at various densities. The heat capacity was derived by interpolation of the internal energy and subsequent differentiation with respect to temperature. For low temperatures of $T \leqslant 30\,000$ K, all curves approach constant values between 4.3–4.8 k_b/atom, which reflects electronic excitations in the metallic liquid and kinetic plus potential contributions from the nuclear motion. At very high temperature where aluminum is fully ionized, we recover the expected nonrelativistic limit of $21k_b = 3/2\ N\ k_b$ where $N = 14$ is the number of free particles (one nucleus and 13 electrons).

For $T \geqslant 10^5$ K, the heat capacity increases as electrons become free. At lower density, this rise occurs slightly faster due to Saha ionization equilibrium favoring free electrons. For the density range of 0.5−12.0 ρ_0, we see a well defined maximum in c_v at $T \approx 5 \times 10^6$ K, which reflects the ionization of K-shell electrons. For low densities of $\rho_0 < 0.5$, this ionization peak shifts to lower temperatures, again due to Saha ionization equilibrium.

IV. SHOCK COMPRESSION

Dynamic shock compression experiments allow one to directly measure the equation of state and other physical properties of hot, dense fluids. Such experiments are often used to determine the principal Hugoniot curve, which is the locus of final states that can be obtained from different shock velocities.

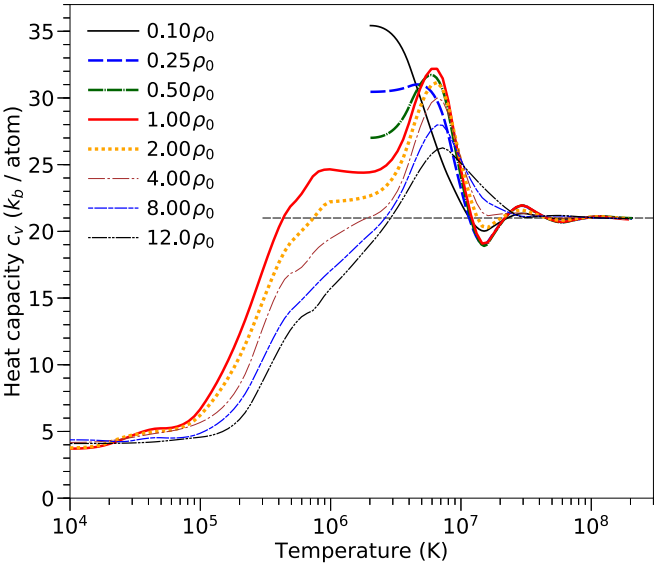

FIG. 5. The heat capacity of aluminum, spanning the warm dense matter and plasma regimes, derived from DFT-MD and PIMC calculations.

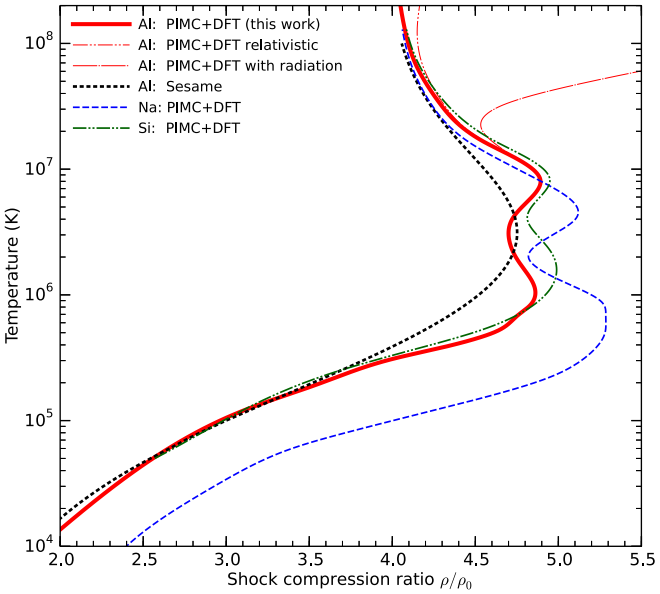

FIG. 6. (a) Comparison of the combined PIMC and DFT-MD shock Hugoniot curve with SESAME-1100 [49], in T-ρ/ρ_0 space. As in Fig. 1, PIMC and DFT-MD predict shell structure effects along the Hugoniot, while SESAME predicts the average ionization behavior, without distinct shell effects.

Density functional theory has been validated by experiments as an accurate tool for predicting the shock compression of a variety of different materials [106–108].

During a shock wave experiment, a material whose initial state is characterized by an internal energy, pressure, and volume, (E_0, P_0, V_0), will change to a final state denoted by (E, P, V) while conserving mass, momentum, and energy. This leads to the Rankine-Hugoniot relation [109],

$$(E - E_0) + \tfrac{1}{2}(P + P_0)(V - V_0) = 0. \qquad (2)$$

Here, we solve this equation for our computed first-principles EOS data set, which is reported in the Supplemental Material [103]. We obtain a continuous Hugoniot curve by interpolating the EOS data with a rectangular-bivariate spline as a function of ρ and T. We have compared several different spline algorithms and find the differences are negligible given that reasonable selections are made for the isochore densities with respect to Hugoniot features. In order to obtain the principal Hugoniot curve, we used the initial condition based on the energy and pressure of ambient, solid, f.c.c. aluminum computed with static DFT ($P_0 = 0.0$ GPa, $E_0 = -241.442$ Ha/atom, $V_0 = 16.603$ Å^3/atom, $\rho_0 = 2.70$ g cm^{-3}).

The resulting Hugoniot curve has been plotted in P-ρ space in Fig. 1, in T-P space in Fig. 2, and in T-ρ/ρ_0 space in Fig. 6. In the high-temperature limit, the Hugoniot curve converges to a compression ratio of 4, which is the value of a nonrelativistic, ideal gas. We also show the magnitude of the relativistic and radiation corrections to the Hugoniot in the high-temperature limit. The shock compression and structure along the Hugoniot is determined by the excitation of internal degrees of freedom, such as dissociation and ionization processes, which increases the compression, and, in addition, by the interaction effects, which decrease the compression [110].

In the structure of the principal Hugoniot curves, we identify two pronounced compression maxima corresponding to ionization of the L-shell and K-shell. The L-shell maximum occurs at $\rho/\rho_0 = 4.86$, $T = 1.1 \times 10^6$ K (94.8 eV), and $P = 0.34$ Gbar. The L-shell peak temperature is consistent with the atomic ionization energies, where the final ionization energy of the M shell is 28.4 eV and the first ionization energy of L shell is 120 eV [111]. Similarly, the K-shell maximum occurs at $\rho/\rho_0 = 4.90$, $T = 7.3 \times 10^7$ K (628.0 eV), and $P = 3.6$ Gbar. Likewise, the K-shell peak temperature is consistent with atomic ionization energies, where the final ionization energy of the L shell is 442 eV and the first ionization energy of the K shell is 2086 eV. Propagating errors from our equation of state data, we estimate that the statistical uncertainly along the Hugoniot curve is at most 4% in the density and 3% in the pressure.

In both Fig. 1 and Fig. 6, we compare our combined PIMC and DFT-MD principal Hugoniot curve with several, widely used EOS tables, such as SESAME (Table 1100) [49,112] and QEOS [50,73], and models, including activity expansion (ACTEX) [56], extended-plane-wave DFT [70], and average atom methods (Purgatorio [64] and pseudoatom MD (PAMD) [68]). The SESAME and QEOS tables are largely dependent on the Thomas-Fermi model, which treats electrons in an ion-sphere as a nonuniform electron gas, neglecting quantum shell effects. Therefore, we see that, while the SESAME and QEOS Hugoniot curves have a rough overall agreement with PIMC and DFT-MD, they do not exhibit any compression maximum related to shell structure. The free energy expansion model, ACTEX, is a semianalytic plasma model parameterized by spectroscopic data, which allows it to incorporate effects of shell structure accurately in the weak-coupling regime (K-shell ionization regime), but less accurately in strong-coupling regime (L-shell ionization regime). The DFT extended-plane-wave and DFT-based average-atom methods compute the shell structure from first-principles and, thus, predict ionization features in good agreement with PIMC. The DFT-based average atom and extended-plane-wave methods tend to predict slightly softer compression in the L-shell ionization regime and stiffer compression in the K-shell ionization regime compared to PIMC.

We compare computed Hugoniot curves with experimental data in Fig. 1. Experimental data is available in the Gbar regime from nuclear tests and at various lower pressures from shock experiments. All models agree reasonably well with the low-pressure experimental shock data. Near the L-shell compression maxima, QEOS predicts a much stiffer response, while ACTEX predicts a significantly softer response compared with the experimental data and first-principles-based models.

In Fig. 7 we compare an isentrope with various multishock Hugoniot curves in order to determine how closely one can trace an isentrope by breaking up a single shock experiment into multiple smaller shocks. All curves start from ambient density, 144 GPa, and 50 000 K. The isentrope [113] was derived from our EOS table using $\frac{dT}{dV}|_S = -T\frac{dP}{dT}|_V / \frac{dE}{dT}|_V$. For weak shocks, the Hugoniot curve does not deviate much from an isentrope. For strong shocks, a substantial amount of shock heating occurs. The resulting single-shock Hugoniot curves are thus much hotter than an isentrope if both are compared

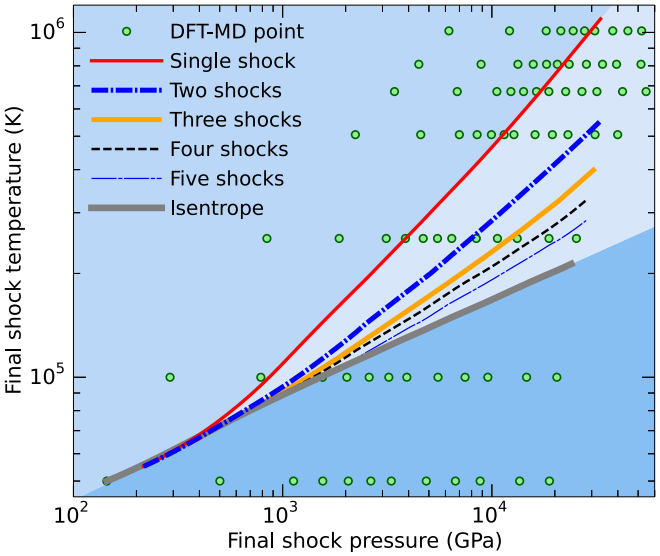

FIG. 7. Comparison of an isentrope and various multishock Hugoniot curves.

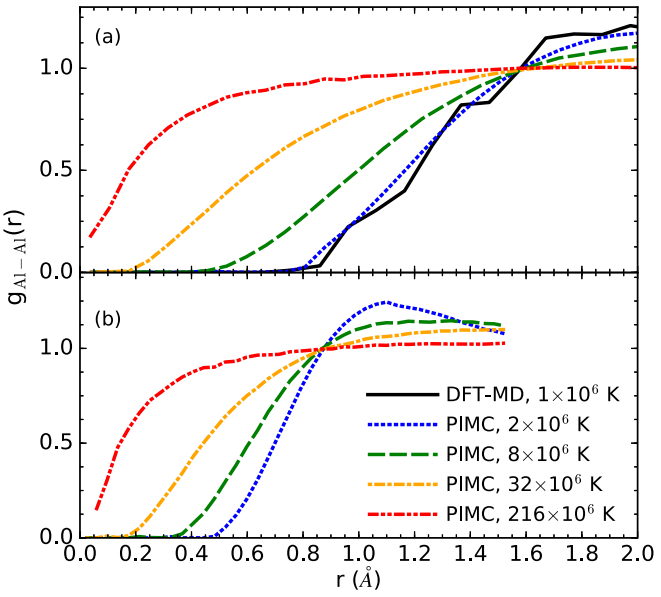

FIG. 8. Pair-correlation functions of Al nuclei computed with PIMC and DFT-MD simulations over a wide range of temperatures in 8-atom simulations cells. Functions are compared for densities of (a) 5.40 (2-fold compression) and (b) 32.38 g cm^{-3} (12-fold compression).

at the same pressure. The discrepancy depends significantly on pressure, which reflects the fact that the final shock density cannot exceed ∼5-fold the initial density (Fig. 1). To reach a large final shock pressure, a substantial pressure contribution must come from the thermal pressure, which requires high temperatures.

One can, however, get arbitrarily close to isentropic compression by breaking up a single shock experiment into multiple weaker shocks. The purpose of Fig. 7 is to assess quantitatively how well this method works for shocks in aluminum and to determine the extent to which shock heating still occurs if the shock is broken up into $N = 2$–5 steps. In our multishock calculations, we successively solve Eq. (2) to connect the intermediate shock states. In order to obtain the lowest possible shock temperature for a given number of shocks, we keep the final shock pressure fixed while we carefully adjust the temperatures of the intermediate shocks until we determined the global minimum of the final shock temperature with sufficient accuracy.

As expected, all the resulting multishock Hugoniot curves converge to an isentrope for weak shocks. For strong shocks such as $P_{\text{final}}/P_{\text{initial}} = 100$, we find the temperature of single-shock temperature is 3.22 times higher than the corresponding temperature on the isentrope. If this shock is broken up into two, well-chosen smaller shocks, the final shock temperature is reduced to 1.87 times the value on the isentrope. If three, four, or five shocks are employed the final shock temperature can, respectively, be reduced to 1.46, 1.30, and 1.22 times the isentropic value, which are substantial reductions compared to the single-shock temperatures.

V. PAIR-CORRELATION FUNCTIONS

In this section, we provide a discussion of the temperature and density dependence of various pair-correlation functions, $g(r)$, in warm dense aluminum. The radial pair correlation function is defined as

$$g(r) = \frac{V}{4\pi r^2 N^2}\left\langle \sum_{j>i} \delta(r - |\vec{r}_i - \vec{r}_j|)\right\rangle, \tag{3}$$

where N is the total number of particles, and V is the cell volume.

Figure 8 shows the temperature dependence of the nuclear pair correlation functions for 2- and 12-fold compression. At low temperatures, the atoms are kept farthest apart, as expected. As temperature increases, kinetic energy of the nuclei increases, leading to stronger collisions and making it more likely to find them at close range. At the same time, the atoms become increasingly ionized, which gradually reduces the Pauli repulsion, while increasing the ionic Coulomb repulsion. In comparison, the likelihood of finding two nuclei at close range rises only slightly, as density increases. At the highest temperatures, the system approaches the Debye-Hückel limit, behaving like a weakly correlated system of screened Coulomb charges. Figure 8(a) shows that we find favorable agreement in the structure as predicted by PIMC at 2×10^6 K and DFT-MD at 1×10^6 K.

Figure 9 shows the integral of the nucleus-electron pair correlation function, $N(r)$, as a function of temperature and density. $N(r)$ provides information about the degree of ionization since it represents the average number of electrons within a sphere of radius r around a given nucleus. $N(r)$ is given by the formula

$$N(r) = \left\langle \frac{1}{N_I} \sum_{e,I} \theta(r - |\vec{r}_e - \vec{r}_I|)\right\rangle, \tag{4}$$

where the sum includes all electron-ion pairs and θ represents the Heaviside function.

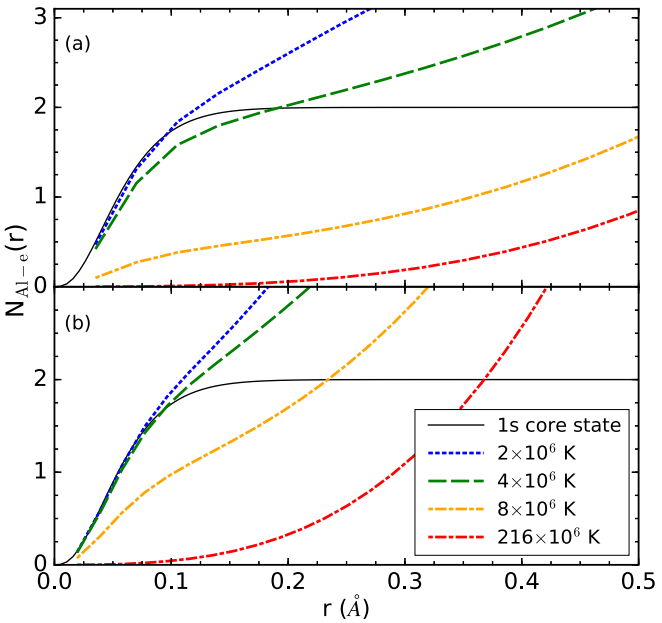

FIG. 9. Number of electrons contained in a sphere of radius, r, around an Al ion. PIMC data at two densities of (a) 5.40 (2-fold compression) and (b) 32.38 g cm^{-3} (12-fold compression) and four temperatures is compared with the doubly occupied Al 1s core ground state (eight-atom simulation cells).

In Fig. 9 we also plot the $N(r)$ function for an isolated Al nucleus with a doubly occupied 1s core state for comparison. We find that the 1s state is fully occupied at 2×10^6 K. As the temperature increases, the 1s state becomes gradually ionized, which drastically reduces the $N(r)$ function at small distance ($r < 0.1$ Å). For given temperature, the degree of ionization is higher at low density. This implies the K-shell ionization is driven by Saha ionization equilibrium in the density range under consideration, as we have observed for other first- and second-row elements in our previous work [86,91]. At higher densities where Pauli exclusion effects between 1s states of different nuclei are of importance, one expects to enter the regime of pressure-driven 1s ionization. However, this is not yet seen in the density regime under consideration.

Figure 10 shows electron-electron pair correlations for electrons having opposite spins. The functions are multiplied by the mass density ρ, so that the integral under the curves is proportional to the number of electrons. This makes it easier to compare $g(r)$ functions of different densities than the usual normalization, $g(r \to \infty) = 1$, in Eq. (3). One finds that the electrons are most highly correlated at low temperatures, which reflects that multiple electrons occupy bound states around a given nucleus. As temperature increases, electrons are thermally excited, decreasing the correlation among each other. The positive correlation at short distances increases with density, consistent with a lower ionization fraction at high density as we have seen in our $N(r)$ plots.

Figure 11 shows electron-electron pair correlations for electrons with parallel spins. The positive correlation at intermediate distances ($r \approx 0.15$ Å) reflects that different electrons with parallel spins are bound to a given nucleus. For short separations, electrons strongly repel due to Pauli exclusion and

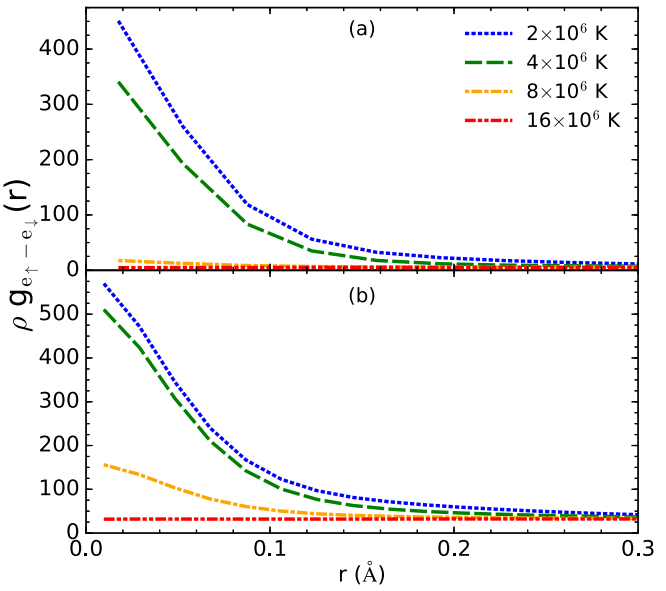

FIG. 10. The electron-electron pair-correlation functions for electrons with opposite spins in PIMC calculations of Al plasma. Results are compared for densities of (a) 5.40 (2-fold compression) and (b) 32.38 g cm^{-3} (12-fold compression).

the functions decay to zero. As density increases, the peak at intermediate distances decreases and clearly shows the effect of pressure ionization of the L shell. Pressure ionization is expected for L-shell orbitals because they are much larger than the K-shell orbitals and are therefore subject to Pauli exchange with nearby nuclei. As temperature increases, more electrons become free, which causes their correlation to diminish except for at very small distances ($r < 0.10$ Å).

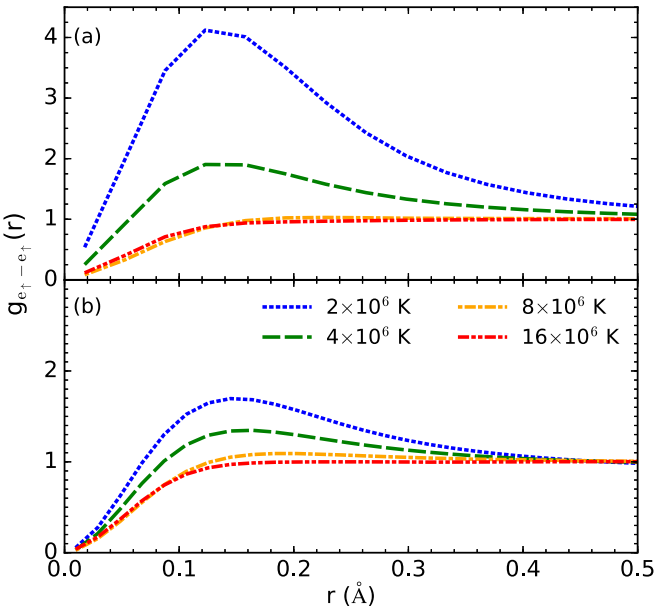

FIG. 11. The electron-electron pair-correlation functions for electrons with parallel spins in PIMC calculations of Al plasma. Results are compared for densities of (a) 5.40 (2-fold compression) and (b) 32.38 g cm^{-3} (12-fold compression).

VI. ELECTRONIC DENSITY OF STATES AND IONIZATION BEHAVIOR

In this section, we report DFT-MD results for the electronic density of states (DOS), binding energies, and the average charge state of aluminum at various temperature-density conditions. This analysis provides further insight into the temperature-density evolution of ionization effects important for continuum lowering [29,114]. All DOS calculations were well-converged in 64-atom simulation cells and $2 \times 2 \times 2$ Monkhorst-Pack k-point sampling. Smooth curves were obtained by averaging over MD-simulation snapshots and applying a Gaussian smearing of 0.5 eV to the band energies. All snapshots were initially aligned at the Fermi energy, averaged together, and then the average Fermi energy was subtracted out. The integral of each occupied DOS is normalized to 1. Our general DOS structures display two peaks, representing bound $2s$ and $2p$ electrons, followed by the valence band gap and a continuum of conducting states. Since our pseudopotential has a frozen $1s$ core, we did not show these states in the DOS plots.

Figure 12 shows the effects of varying density and temperature independently on the occupied DOS. As density increases at a fixed temperature in Fig. 12(a), the DOS peaks and the Fermi energy are both upshifted. However, the Fermi energy upshifts at a faster rate than the peaks, and, therefore, the $2s$ and $2p$ binding energies increase with density. We also note a significant peak-broadening effect as density increases. On the other hand, as temperature increases at a fixed density in Fig. 12(b), thermal ionization reduces the electronic screening of the ions, which downshifts the DOS peaks and the Fermi energy. However, the Fermi energy downshifts at a faster rate than the peaks, and, therefore, the $2s$ and $2p$ binding energies decrease with temperature, which is the opposite effect of density. We note that we found similar edge and Fermi shift behavior in our previous study of warm dense oxygen [86], and recent work by others on optical properties of dense CH [115,116] and iron [117,118] report similar effects.

Figure 13 shows the total and occupied DOS at five density-temperature points chosen along the principal Hugoniot curve. As the density and temperature increase simultaneously along the Hugoniot curve, competing electronic effects determine the net shift in the DOS peak location, consistent with the behavior presented in Fig. 12. Comparing DOS peaks for the lowest two density-temperature conditions, the peaks shift to slightly higher energies and, thus, their positions are dominated by the density change, as the temperature is not yet high enough to have ionized the L shell. For the higher density-temperature conditions, the L shell begins to ionize and temperature effects begin to dominate the DOS shift, causing the DOS peaks to shift towards lower energies. When the temperature reaches 10^6 K, the peaks have shifted nearly 50 eV lower in energy. The Fermi energies, marked by style-matched vertical lines, downshift more rapidly, such that the $2s$- and $2p$-ionization energies significantly decrease along the Hugoniot path. We

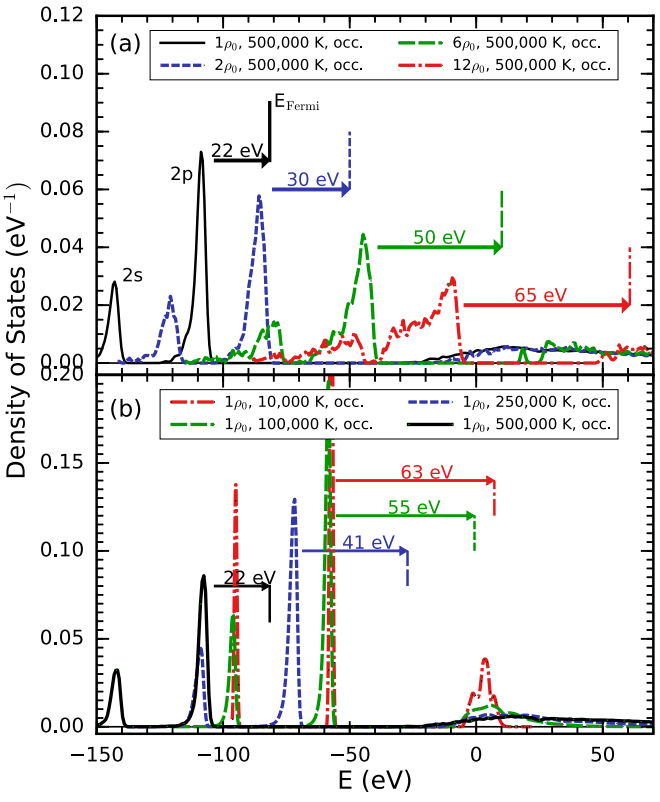

FIG. 12. (a) Density-driven upshifting of the occupied DOS and Fermi energy at a fixed temperature of 5×10^5 K. (b) Temperature-driven downshifting of the occupied DOS and Fermi energy at a fixed, ambient density.

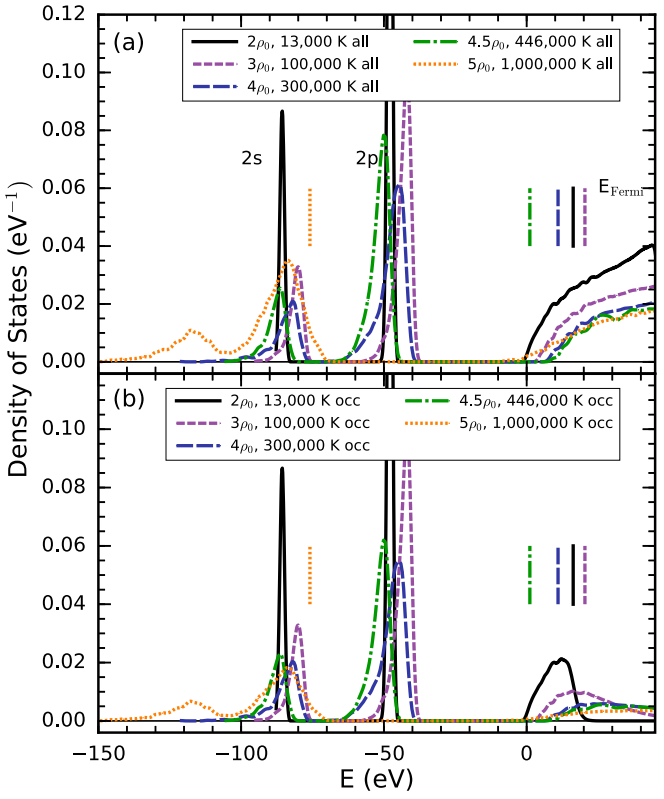

FIG. 13. The computed (a) total (all) and (b) occupied (occ.) electronic DOS at rho-T conditions along the principal Hugoniot curve from DFT-MD. The Fermi energies are marked by vertical lines with colors and line-styles corresponding to their respective DOS curve.

also note peak broadening of the bound electronic states due to compression and thermal fluctuations.

In Fig. 12(b) we also note that the near-ambient ionization energy is roughly 63 eV for our DFT-MD(LDA) calculation. This value is lower than the ambient, experimentally measured value of 72.7 eV [119]. It is well known that standard Kohn-Sham DFT is often inaccurate for computing band gaps of insulators and semiconductors near the ground state, which can sometimes be corrected by using advanced hybrid functionals [120] or the GW approximation [121]. Previous DFT ionization energy calculations [122] using the PBE (64.7 eV) and the hybrid HSE (68.9 eV) functional improve agreement with experiment in this case at near-ambient conditions.

However, we do not expect the uncertainty in our computed, LDA ionization energy to significantly alter the effects of ionization in our EOS or Hugoniot curve results. We first note that corrections to DFT band gaps are expected to become much less significant as temperature increases [123]. Second, since the DFT error in the ionization energy is very small relative to the total internal energy, especially at higher temperatures, one does not expect an ionization-energy uncertainty to significantly affect our overall EOS or Hugoniot curve results. Additionally, we note that when one considers density and temperature effects on the DOS separately, the shifts in the DOS are larger than the uncertainty in the ionization energy, as was shown in Fig. 12. Therefore, the onset of thermal or pressure ionization, which affects the location of the L-shell compression peak in our Hugoniot curves, is not expected to be overly sensitive to the DFT ionization energy uncertainty. Hence, there is little motivation to expect improvements in the EOS or ionization behavior by applying advanced band-gap corrections to DFT. We also note that PIMC does not suffer from the band gap problem and the ionization energy uncertainty is a small part of the small, 1–4 Ha/atom, internal energy differences we find between DFT and PIMC near $T \sim 1 \times 10^6$ K.

In Fig. 14 we report the DFT-MD valence band gap width as a function of compression at $T = 8.6$ eV. The error bars, in the two points shown at 1- and 12-fold compression, represent a four-sigma statistical error computed from approximately 20 snapshots. These results show that the DFT-MD valence band gap only decreases slightly with compression over the compression range. There is no expectation for the band gap to go to zero monotonically, as can be seen in the upshifting behavior of core states in other works [86,115,116]. The fact that the band gap does not go to zero over the examined compression range means that DFT-MD does not predict any pressure ionization of the L shell for 12-fold compression or lower. We juxtapose our DFT-MD curve with atomic ionization energy calculations from a recent atomic-kinetics model (REODP) [124] that incorporates continuum lowering based on the ion-sphere model known as Stewart-Pyatt [125]. The results differ in that the atomic models predict that the ionization energy goes to zero before 12-fold compression, indicating L-shell pressure ionization.

This discrepancy between the DFT-MD and atomic model predictions of pressure ionization is likely due to approximate ways that models introduce ionization potential depression. The continuum lowering models, such as Stewart-Pyatt, are

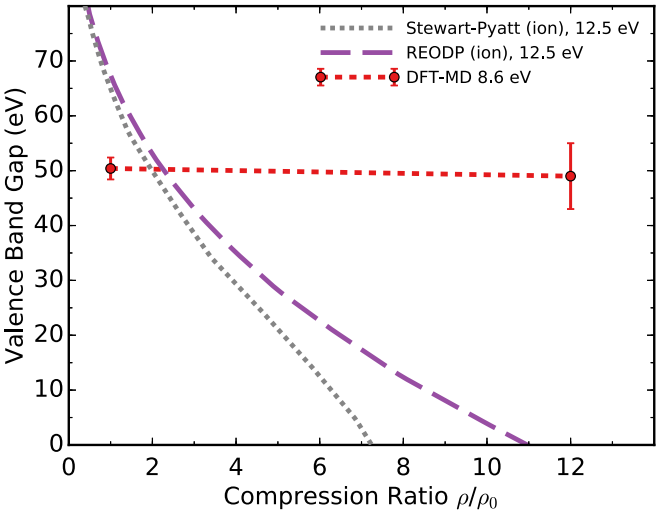

FIG. 14. The valence band gap, computed with DFT-MD as a function of compression ratio at fixed temperature 8.6 eV. Results are compared with 2p-ionization energies from REODP and Stewart-Pyatt models for the isolated atom at a temperature of 12.5 eV [124].

generally based on an isolated-atom picture that is only valid in the low-density plasma regime. We also note that the atomic ionization energy difference in Fig. 14 is taken with respect to a fixed, ground state Al3+ ionization potential. That is, the continuum level is fixed in an the isolated atomic calculations. DFT-MD, on the other hand, provides a self-consistent, first-principles treatment of dynamic ion interactions and their effect on electronic structure. The continuum is treated dynamically in DFT with those states maintaining orthogonality to the shifting bound states. Therefore, DFT-MD predictions for dense, many-body systems are generally considered to be more reliable than atomic models. We note that recent, high-resolution spectroscopy data for highly compressed iron [117] show that K-edge shifts are in good agreement with DFT-MD and not in agreement with the common atomic models for ionization depression, such as Stewart-Pyatt.

However, it should be noted that DFT-MD calculations can be limited in accuracy by the pseudopotential, which, in the present study, has a frozen 1s core and a 1.7 Bohr cutoff radius. The nearest-neighbor ion distances at 12-fold compression can be as low as 1.5 Bohr, while our pseudopotential only guarantees the proper charge density between ions for separations >1.7 Bohr. By including 4-sigma error bars in Fig. 14, we acknowledge that DFT band gaps have some room for improvement, as usual, but there is no indication that the gap is close to zero in the considered range. We did spot-check our 12-fold DFT-MD band gap calculation with our more expensive 0.6 Bohr cutoff radius pseudopotential and found identical results. We have also carefully tested the integrity of our results for k-point convergence. We expect the effects of 1s-core upshifting, given one had an all-electron potential, would have a small effect on the computed gaps. And, ultimately, the consistency of our DFT-MD results with all-electron PIMC results, even at 12-fold compression, indicates that DFT-MD errors are likely small.

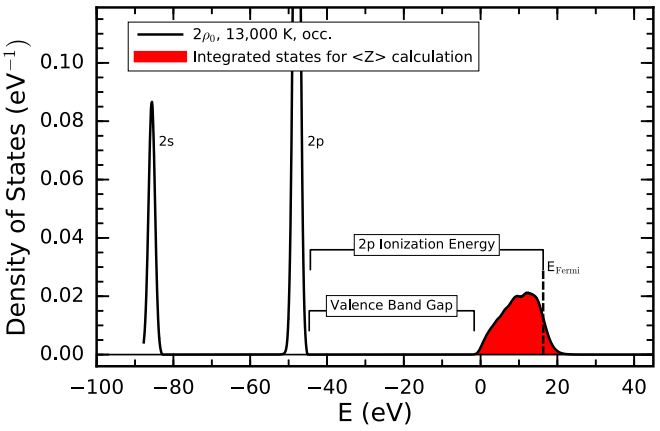

FIG. 15. An example DOS showing that $\langle Z \rangle$ is computed by integrating occupied conducting states above the valence band gap, which is shaded red for clarity.

In order to further characterize the ionization behavior predicted by our DFT-MD (LDA) and PIMC simulations, we also examine the average ionic charge, $\langle Z \rangle$. In our method of extracting $\langle Z \rangle$ from DFT-MD simulations, we integrate the occupied DOS above the valence band gap, which is visualized at the red-shaded area in Fig. 15. We also compute $\langle Z \rangle$ from the higher temperature PIMC results by extracting the occupation fraction of the 1s state from the $N(r < 0.1$ Å) functions in Fig. 9. We only considered PIMC results where all other bound states are fully ionized. Combining the DFT and PIMC analysis allows us to construct a coherent $\langle Z \rangle$ across the ambient, WDM, and fully plasma regimes.

Figure 16 shows $\langle Z \rangle$ as a function of temperature computed from DFT-MD and PIMC at densities corresponding to ambient and 12-fold compression. Our $\langle Z \rangle$ at ambient density compares well with various models (SESAME, QEOS, REODP) that are based on ion-sphere continuum lowering approaches. The good agreement of our $\langle Z \rangle$ with other models helps to confirm the accuracy of our DFT-MD ionization energies, and, therefore, the accuracy of our EOS and Hugoniot curve. For a given temperature, the $\langle Z \rangle$ at higher density is always less than at lower density, which is consistent with ionization trends discussed in Fig. 12 and Fig. 14. We noted that in addition to the effect of the Fermi shift on ionization, there is also substantial density-driven peak broadening of the DOS, which further reinforces the ionization trends.

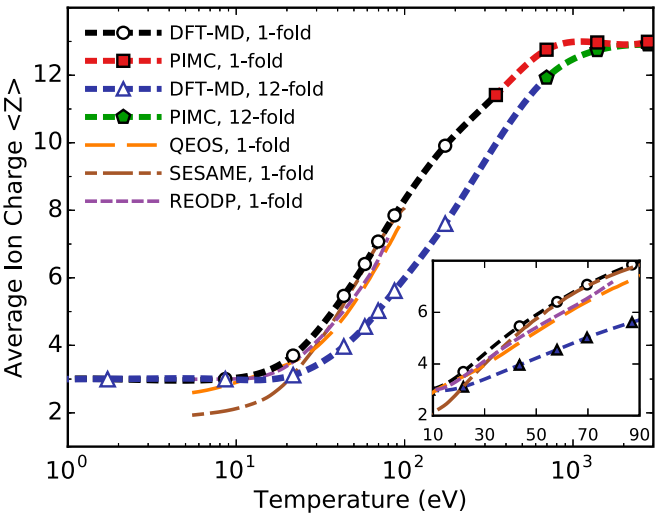

FIG. 16. $\langle Z \rangle$ as a function of temperature, computed from our DFT-MD and PIMC simulations, for densities corresponding to ambient (2.70 g cm^{-3}) and 12-fold (32.38 g cm^{-3}) compression. The results are compared with a variety of other models at ambient density conditions. The inset shows a zoom-in of the comparisons.

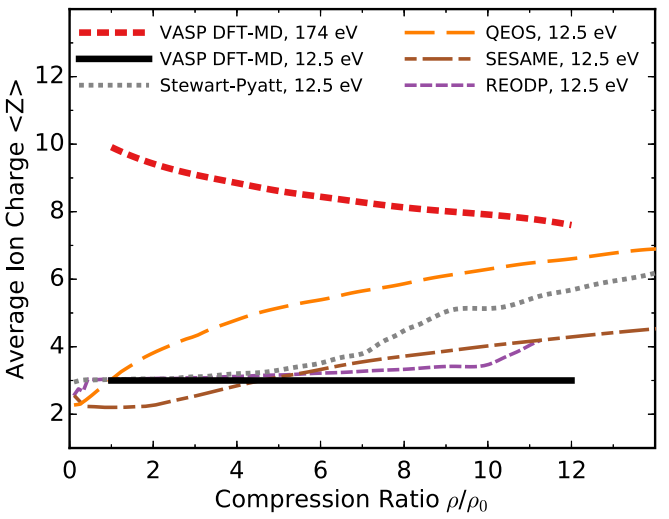

FIG. 17. $\langle Z \rangle$ as a function of compression, computed from our DFT-MD and PIMC simulations, for temperatures of 12.5 and 174 eV. The results are compared with a variety of other models evaluated a temperature of 12.5 eV.

Additionally, Fig. 17 shows $\langle Z \rangle$ as a function of compression. For the lower temperature curve and for low densities, our DFT-MD results compare well with the same variety of models (QEOS, SESAME, Stewart-Pyatt, and REODP). As we noted previously in Fig. 14, the continuum lowering models predict pressure ionization before 12-fold compression, while DFT-MD does not predict any pressure ionization over the same range. Hence, the low-temperature DFT-MD curve stays constant at the ground state $\langle Z \rangle$ of 3, while the other models show $\langle Z \rangle$ increasing due to pressure ionization. At high-temperature, DFT-MD curve shows $\langle Z \rangle$ decreasing with compression. This result is consistent with the result of Fig. 12(a), which shows that the Fermi energy upshifts more rapidly than the L-shell energies under compression at a fixed temperature. Therefore, it is more difficult to *temperature*-ionize the L shell at higher densities.

Generally, several effects may contribute to discrepancies between DFT-MD and atomic ionization models. First, we note there is no rigorous way to derive $\langle Z \rangle$ from a many-body wave function at high density [126]. $\langle Z \rangle$ is well defined in a low-density plasma state, where there is little hybridization of the atomic orbitals. At high density and temperature, the electrons partially occupy states in broad energy bands that span many atoms. For this reason, it is challenging to separate bound and free electrons to derive a consistent $\langle Z \rangle$. As noted by Hansen *et al.* [117], particular codes differ in their implementation of ionization potential depression models and they often

have idiosyncratic choices for electronic state deconstruction between bound and unbound states. These choices likely play a significant role in the differences observed between the various models in Fig. 17.

VII. CONCLUSIONS

In this paper, we have constructed a first-principles EOS of aluminum over a wide temperature-density range with DFT-MD and PIMC. We used constructed a coherent EOS that bridges the WDM and plasma regimes. We showed that both PIMC and DFT-MD produce consistent EOS data at $T = 2 \times 10^6$ K, validating the use of the fixed-node approximation in PIMC and zero-temperature XC functionals in DFT-MD for warm dense aluminum. We examined the shock compression behavior of aluminum and computed a first-principles benchmark for the principal Hugoniot. We compare our PIMC Hugoniot results with widely used Thomas-Fermi-based models, which do not include shell effects and DFT-based models, which show the same trends as we observe in PIMC, with only small differences in compression. Subsequently, we showed a multishock analysis can allow one to get arbitrarily close to isentropic compression. Finally, we then studied heat capacity, pair-correlation functions, electronic density of states, and $\langle Z \rangle$ to reveal the evolution of the plasma structure and ionization behavior. Overall, we demonstrate that PIMC is an important tool to benchmark the EOS in the WDM regime. Kohn-Sham based DFT simulations are not efficient enough to access physics at temperatures corresponding to the core ionization, and the more efficient, but approximate models do not necessarily capture all of the complex physics of the WDM regime.

ACKNOWLEDGMENTS

We thank Gérard Massacrier for insightful discussions. This research was supported by the U.S. Department of Energy under Grants No. DE-SC0010517 and No. DE-SC0016248. This work was also performed under the auspices of the U.S. Department of Energy by Lawrence Livermore National Laboratory under Contract No. DE-AC52-07NA27344. This document was prepared as an account of work sponsored by an agency of the United States government. Neither the United States government nor Lawrence Livermore National Security, LLC, nor any of their employees makes any warranty, expressed or implied, or assumes any legal liability or responsibility for the accuracy, completeness, or usefulness of any information, apparatus, product, or process disclosed, or represents that its use would not infringe privately owned rights. Reference herein to any specific commercial product, process, or service by trade name, trademark, manufacturer, or otherwise does not necessarily constitute or imply its endorsement, recommendation, or favoring by the United States government or Lawrence Livermore National Security, LLC. The views and opinions of authors expressed herein do not necessarily state or reflect those of the United States government or Lawrence Livermore National Security, LLC, and shall not be used for advertising or product endorsement purposes. Computational support was provided by the Blue Waters sustained-petascale computing project (NSF ACI 1640776), which is supported by the National Science Foundation (Awards OCI-0725070 and ACI-1238993) and the state of Illinois. Blue Waters is a joint effort of the University of Illinois at Urbana-Champaign and its National Center for Supercomputing Applications. This research also used resources of the National Energy Research Scientific Computing Center, a DOE Office of Science User Facility supported by the Office of Science of the U.S. Department of Energy under Contract No. DE-AC02-05CH11231.

[1] T. Guillot, Annu. Rev. Earth Planet. Sci. **33**, 493 (2005).
[2] G. Wallerstein, I. Iben, P. Parker, A. M. Boesgaard, G. M. Hale, A. E. Champagne, C. A. Barnes, F. Käppeler, V. V. Smith, R. D. Hoffman *et al.*, Rev. Mod. Phys. **69**, 995 (1997).
[3] R. Betti and O. Hurricane, Nat. Phys. **12**, 435 (2016).
[4] N. Meezan, M. Edwards, O. Hurricane, P. Patel, D. Callahan, W. Hsing, R. Town, F. Albert, P. Amendt, L. B. Hopkins *et al.*, Plasma Phys. Controlled Fusion **59**, 014021 (2016).
[5] V. Goncharov, S. Regan, E. Campbell, T. Sangster, P. Radha, J. Myatt, D. Froula, R. Betti, T. Boehly, J. Delettrez *et al.*, Plasma Phys. Controlled Fusion **59**, 014008 (2016).
[6] M. J. Tambe, N. Bonini, and N. Marzari, Phys. Rev. B **77**, 172102 (2008).
[7] C. J. Pickard and R. Needs, Nat. Mater. **9**, 624 (2010).
[8] L. Al'Tshuler, S. Kormer, A. Bakanova, and R. Trunin, Sov. Phys. JETP **11**, 573 (1960).
[9] L. Al'Tshuler, N. Kalitkin, L. Kuzmina, and B. Chekin, Sov. Phys. JETP **45**, 167 (1977).
[10] C. E. Ragan III, Phys. Rev. A **25**, 3360 (1982).
[11] A. Vladimirov, N. Voloshin, V. Nogin, A. Petrovtsev, and V. Simonenko, JETP Lett. **39**, 82 (1984).
[12] E. Avrorin, B. Vodolaga, N. Voloshin, G. Kovalenko, V. Kuropatenko, V. Simonenko, and B. Chernovolyuk, Sov. Phys. JETP **93**, 347 (1987).
[13] V. Simonenko, N. Voloshin, S. Vladirmirov, P. Nagibin, and V. Nogin, Zh. Eksp. Teor. Fiz **88**, 1452 (1985).
[14] W. J. Nellis, J. A. Moriarty, A. C. Mitchell, M. Ross, R. G. Dandrea, N. W. Ashcroft, N. C. Holmes, and G. R. Gathers, Phys. Rev. Lett. **60**, 1414 (1988).
[15] M. D. Knudson, R. Lemke, D. Hayes, C. A. Hall, C. Deeney, and J. Asay, J. Appl. Phys. **94**, 4420 (2003).
[16] P. Celliers, G. Collins, D. Hicks, and J. Eggert, J. Appl. Phys. **98**, 113529 (2005).
[17] S. Regan, H. Sawada, V. Goncharov, D. Li, P. Radha, R. Epstein, J. Delettrez, S. Hu, V. Smalyuk, B. Yaakobi *et al.*, High Energy Density Phys. **7**, 259 (2011).
[18] M. D. Knudson, M. P. Desjarlais, and A. Pribram-Jones, Phys. Rev. B **91**, 224105 (2015).
[19] L. Lecherbourg, P. Renaudin, S. Bastiani-Ceccotti, J.-P. Geindre, C. Blancard, P. Cossé, G. Faussurier, R. Shepherd, and P. Audebert, High Energy Density Phys. **3**, 175 (2007).

[20] A. Ravasio, G. Gregori, A. Benuzzi-Mounaix, J. Daligault, A. Delserieys, A. Y. Faenov, B. Loupias, N. Ozaki, M. R. Le Gloahec, T. Pikuz *et al.*, Phys. Rev. Lett. **99**, 135006 (2007).

[21] A. Benuzzi-Mounaix, F. Dorchies, V. Recoules, F. Festa, O. Peyrusse, A. Levy, A. Ravasio, T. Hall, M. Koenig, N. Amadou *et al.*, Phys. Rev. Lett. **107**, 165006 (2011).

[22] B. Cho, K. Engelhorn, S. Vinko, H.-K. Chung, O. Ciricosta, D. Rackstraw, R. Falcone, C. Brown, T. Burian, J. Chalupský *et al.*, Phys. Rev. Lett. **109**, 245003 (2012).

[23] S. Vinko, O. Ciricosta, B. Cho, K. Engelhorn, H.-K. Chung, C. Brown, T. Burian, J. Chalupský, R. Falcone, C. Graves *et al.*, Nature (London) **482**, 59 (2012).

[24] O. Ciricosta, S. Vinko, H.-K. Chung, B.-I. Cho, C. Brown, T. Burian, J. Chalupský, K. Engelhorn, R. Falcone, C. Graves *et al.*, Phys. Rev. Lett. **109**, 065002 (2012).

[25] T. Ma, T. Döppner, R. Falcone, L. Fletcher, C. Fortmann, D. O. Gericke, O. Landen, H. Lee, A. Pak, J. Vorberger *et al.*, Phys. Rev. Lett. **110**, 065001 (2013).

[26] D. Hoarty, P. Allan, S. James, C. Brown, L. Hobbs, M. Hill, J. Harris, J. Morton, M. Brookes, R. Shepherd *et al.*, High Energy Density Phys. **9**, 661 (2013).

[27] D. Hoarty, P. Allan, S. James, C. Brown, L. Hobbs, M. Hill, J. Harris, J. Morton, M. Brookes, R. Shepherd *et al.*, Phys. Rev. Lett. **110**, 265003 (2013).

[28] B. Crowley, High Energy Density Phys. **13**, 84 (2014).

[29] S. Vinko, O. Ciricosta, and J. Wark, Nat. Commun. **5**, 3533 (2014).

[30] S.-K. Son, R. Thiele, Z. Jurek, B. Ziaja, and R. Santra, Phys. Rev. X **4**, 031004 (2014).

[31] K.-U. Plagemann, H. R. Rüter, T. Bornath, M. Shihab, M. P. Desjarlais, C. Fortmann, S. H. Glenzer, and R. Redmer, Phys. Rev. E **92**, 013103 (2015).

[32] P. Sperling, E. Gamboa, H. Lee, H. Chung, E. Galtier, Y. Omarbakiyeva, H. Reinholz, G. Röpke, U. Zastrau, J. Hastings *et al.*, Phys. Rev. Lett. **115**, 115001 (2015).

[33] S. M. Vinko, J. Plasma Phys. **81**, 365810501 (2015).

[34] L. Fletcher, H. Lee, T. Döppner, E. Galtier, B. Nagler, P. Heimann, C. Fortmann, S. LePape, T. Ma, M. Millot *et al.*, Nat. Photonics **9**, 274 (2015).

[35] S. Mazevet, M. P. Desjarlais, L. A. Collins, J. D. Kress, and N. H. Magee, Phys. Rev. E **71**, 016409 (2005).

[36] S. Mazevet and G. Zérah, Phys. Rev. Lett. **101**, 155001 (2008).

[37] V. Recoules and S. Mazevet, Phys. Rev. B **80**, 064110 (2009).

[38] B. Nagler, U. Zastrau, R. R. Fäustlin, S. M. Vinko, T. Whitcher, A. Nelson, R. Sobierajski, J. Krzywinski, J. Chalupsky, E. Abreu *et al.*, Nat. Phys. **5**, 693 (2009).

[39] S. M. Vinko, G. Gregori, M. P. Desjarlais, B. Nagler, T. J. Whitcher, R. W. Lee, P. Audebert, and J. S. Wark, High Energy Density Phys. **5**, 124 (2009).

[40] J. Clérouin, P. Noiret, V. N. Korobenko, and A. D. Rakhel, Phys. Rev. B **78**, 224203 (2008).

[41] V. Recoules and J.-P. Crocombette, Phys. Rev. B **72**, 104202 (2005).

[42] G. Faussurier, C. Blancard, P. Cossé, and P. Renaudin, Phys. Plasmas **17**, 052707 (2010).

[43] T. Sjostrom and J. Daligault, Phys. Rev. E **92**, 063304 (2015).

[44] M. Veysman and N. Andreev, J. Phys. Conf. Ser. **653**, 012004 (2015).

[45] C. E. Starrett, J. Daligault, and D. Saumon, Phys. Rev. E **91**, 013104 (2015).

[46] V. V. Karasiev, L. Calderín, and S. B. Trickey, Phys. Rev. E **93**, 063207 (2016).

[47] Y. Hou, Y. Fu, R. Bredow, D. Kang, R. Redmer, and J. Yuan, High Energy Density Phys. **22**, 21 (2017).

[48] R. Jeanloz, P. M. Celliers, G. W. Collins, J. H. Eggert, . K. K. M. Lee, R. S. McWilliams, S. Brygoo, and P. Loubeyre, Proc. Natl. Acad. Sci. USA **104**, 9172 (2007).

[49] S. P. Lyon and J. D. Johnson, Los Alamos Report No. LA-UR-92-3407 (unpublished).

[50] R. More, K. Warren, D. Young, and G. Zimmerman, Phys. Fluids **31**, 3059 (1988).

[51] Q. Porcherot, G. Faussurier, and C. Blancard, High Energy Density Phys. **6**, 76 (2010).

[52] V. Mishra, C. Sijoy, P. Pahari, and S. Chaturvedi, J. Phys. Conf. Ser. **377**, 012105 (2012).

[53] R. F. Trunin, Phys.-Usp. **37**, 1123 (1994).

[54] M. A. Kadatskiy and K. V. Khishchenko, J. Phys. Conf. Ser. **653**, 012079 (2015).

[55] D. Young, J. Wolford, F. Rogers, and K. Holian, Phys. Lett. A **108**, 157 (1985).

[56] F. J. Rogers and D. A. Young, Phys. Rev. E **56**, 5876 (1997).

[57] I. Lomonosov, M. Elert, M. D. Furnish, R. Chau, N. Holmes, and J. Nguyen, in *AIP Conference Proceedings* (AIP, New York, 2007), Vol. 955, pp. 63–66.

[58] R. Davydov, V. Antonov, and N. Kalinin, J. Phys. Conf. Ser. **643**, 012107 (2015).

[59] M. Zaghloul, High Energy Density Phys. **26**, 8 (2018).

[60] M. P. Surh, T. W. Barbee III, and L. H. Yang, Phys. Rev. Lett. **86**, 5958 (2001).

[61] D. Minakov, P. Levashov, K. Khishchenko, and V. Fortov, J. Appl. Phys. **115**, 223512 (2014).

[62] X. Gao, L. Chen, R. Valencia, W. Xia, W. Gao, X.-Y. Han, J.-M. Li, and P. Zhang, Phys. Plasmas **23**, 092710 (2016).

[63] T. Sjostrom, S. Crockett, and S. Rudin, Phys. Rev. B **94**, 144101 (2016).

[64] B. Wilson, V. Sonnad, P. Sterne, and W. Isaacs, J. Quant. Spectrosc. Radiat. Transfer **99**, 658 (2006).

[65] J. Pain, Phys. Lett. A **362**, 120 (2007).

[66] M. Pénicaud, J. Phys.: Condens. Matter **21**, 095409 (2009).

[67] R. Piron and T. Blenski, Phys. Rev. E **83**, 026403 (2011).

[68] C. E. Starrett and D. Saumon, Phys. Rev. E **93**, 063206 (2016).

[69] F. Lambert, J. Clérouin, and G. Zérah, Phys. Rev. E **73**, 016403 (2006).

[70] S. Zhang, H. Wang, W. Kang, P. Zhang, and X. He, Phys. Plasmas **23**, 042707 (2016).

[71] B. F. Rozsnyai, J. R. Albritton, D. A. Young, V. N. Sonnad, and D. A. Liberman, Phys. Lett. A **291**, 226 (2001).

[72] P. Renaudin, C. Blancard, J. Clérouin, G. Faussurier, P. Noiret, and V. Recoules, Phys. Rev. Lett. **91**, 075002 (2003).

[73] D. A. Young and E. M. Corey, J. Appl. Phys. **78**, 3748 (1995).

[74] K. P. Driver and B. Militzer, Phys. Rev. Lett. **108**, 115502 (2012).

[75] B. Militzer and K. P. Driver, Phys. Rev. Lett **115**, 176403 (2015).

[76] D. Ceperley, J. Stat. Phys. **63**, 1237 (1991).

[77] D. M. Ceperley, Rev. Mod. Phys. **67**, 279 (1995).

[78] D. M. Ceperley, in *Monte Carlo and Molecular Dynamics of Condensed Matter Systems*, edited by K. Binder and G. Ciccotti (Editrice Compositori, Bologna, Italy, 1996), Vol. 49, p. 443.

[79] R. Car and M. Parrinello, Phys. Rev. Lett. **55**, 2471 (1985).

[80] M. C. Payne, M. P. Teter, D. C. Allan, T. Arias, and J. Joannopoulos, Rev. Mod. Phys. **64**, 1045 (1992).
[81] D. Marx and J. Hutter, *Ab Initio Molecular Dynamics: Basic Theory and Advanced Methods* (Cambridge University Press, Cambridge, 2009).
[82] B. Militzer and D. M. Ceperley, Phys. Rev. E **63**, 066404 (2001).
[83] B. Militzer, Phys. Rev. B **79**, 155105 (2009).
[84] L. X. Benedict, K. P. Driver, S. Hamel, B. Militzer, T. Qi, A. A. Correa, A. Saul, and E. Schwegler, Phys. Rev. B **89**, 224109 (2014).
[85] K. P. Driver and B. Militzer, Phys. Rev. B **91**, 045103 (2015).
[86] K. Driver, F. Soubiran, S. Zhang, and B. Militzer, J. Chem. Phys. **143**, 164507 (2015).
[87] D. Okuyama, K. Shibuya, R. Kumai, T. Suzuki, Y. Yamasaki, H. Nakao, Y. Murakami, M. Kawasaki, Y. Taguchi, Y. Tokura, and T. Arima, Phys. Rev. B **91**, 064101 (2015).
[88] S. X. Hu, B. Militzer, L. A. Collins, K. P. Driver, and J. D. Kress, Phys. Rev. B **94**, 094109 (2016).
[89] S. Zhang, K. P. Driver, F. Soubiran, and B. Militzer, High Energy Density Phys. **21**, 16 (2016).
[90] S. Zhang, K. P. Driver, F. Soubiran, and B. Militzer, J. Chem. Phys. **146**, 074505 (2017).
[91] K. P. Driver, F. Soubiran, S. Zhang, and B. Militzer, High Energ. Dens. Phys. **23**, 81 (2017).
[92] K. P. Driver and B. Militzer, Phys. Rev. E **95**, 043205 (2017).
[93] S. Zhang, K. P. Driver, F. Soubiran, and B. Militzer, Phys. Rev. E **96**, 013204 (2017).
[94] C. Pierleoni, D. M. Ceperley, B. Bernu, and W. R. Magro, Phys. Rev. Lett. **73**, 2145 (1994).
[95] G. Kresse and J. Furthmüller, Phys. Rev. B **54**, 11169 (1996).
[96] P. E. Blöchl, Phys. Rev. B **50**, 17953 (1994).
[97] G. Kresse and D. Joubert, Phys. Rev. B **59**, 1758 (1999).
[98] D. M. Ceperley and B. J. Alder, Phys. Rev. Lett. **45**, 566 (1980).
[99] M. P. Allen and D. J. Tildesley, *Computer Simulation of Liquids* (Oxford University Press, Oxford, 2017).
[100] X. Gonze, B. Amadon, P. M. Anglade, J. M. Beuken, F. Bottin, P. Boulanger, F. Bruneval, D. Caliste, R. Caracas, M. Côté *et al.*, Comput. Phys. Commun. **180**, 2582 (2009).
[101] N. A. W. Holzwarth, A. R. Tackett, and G. E. Matthews, Comput. Phys. Commun. **135**, 329 (2001).
[102] http://elk.sourceforge.net/.
[103] See Supplemental Material at http://link.aps.org/supplemental/10.1103/PhysRevE.97.063207 for the EOS table.
[104] http://opium.sourceforge.net.
[105] P. Debye and E. Huckel, Phys. Z. **24**, 185 (1923).
[106] S. Root, R. J. Magyar, J. H. Carpenter, D. L. Hanson, and T. R. Mattsson, Phys. Rev. Lett. **105**, 085501 (2010).
[107] X. Wang, F. Tian, L. Wang, T. Cui, B. Liu, and G. Zou, J. Chem. Phys. **132**, 024502 (2010).
[108] T. R. Mattsson, S. Root, A. E. Mattsson, L. Shulenburger, R. J. Magyar, and D. G. Flicker, Phys. Rev. B **90**, 184105 (2014).
[109] Y. B. Zeldovich and Y. P. Raizer, *Elements of Gasdynamics and the Classical Theory of Shock Waves* (Academic Press, New York, 1968).
[110] B. Militzer, Phys. Rev. Lett. **97**, 175501 (2006).
[111] https://www.nist.gov/pml/atomic-spectra-database.
[112] http://www.lanl.gov/org/padste/adtsc/theoretical/physics-chemistry-materials/sesame-database.php.
[113] B. Militzer and W. Hubbard, Astrophys. Space Sci. **322**, 129 (2009).
[114] C. Lin, G. Röpke, W.-D. Kraeft, and H. Reinholz, Phys. Rev. E **96**, 013202 (2017).
[115] S. X. Hu, Phys. Rev. Lett. **119**, 065001 (2017).
[116] S. X. Hu, L. A. Collins, J. P. Colgan, V. N. Goncharov, and D. P. Kilcrease, Phys. Rev. B **96**, 144203 (2017).
[117] S. Hansen, E. Harding, P. Knapp, M. Gomez, T. Nagayama, and J. Bailey, High Energy Density Phys. **24**, 39 (2017).
[118] S. Hansen, E. Harding, P. Knapp, M. Gomez, T. Nagayama, and J. Bailey, Phys. Plasmas **25**, 056301 (2018).
[119] E. M. Gullikson, P. Denham, S. Mrowka, and J. H. Underwood, Phys. Rev. B **49**, 16283 (1994).
[120] J. Heyd, J. E. Peralta, G. E. Scuseria, and R. L. Martin, J. Chem. Phys. **123**, 174101 (2005).
[121] W. G. Aulbur, M. Städele, and A. Görling, Phys. Rev. B **62**, 7121 (2000).
[122] B. B. L. Witte, L. B. Fletcher, E. Galtier, E. Gamboa, H. J. Lee, U. Zastrau, R. Redmer, S. H. Glenzer, and P. Sperling, Phys. Rev. Lett. **118**, 225001 (2017).
[123] S. V. Faleev, M. van Schilfgaarde, T. Kotani, F. Léonard, and M. P. Desjarlais, Phys. Rev. B **74**, 033101 (2006).
[124] G. Miloshevsky and A. Hassanein, Phys. Rev. E **92**, 033109 (2015).
[125] J. C. Stewart and K. D. Pyatt Jr, Astrophys. J. **144**, 1203 (1966).
[126] W. Ebeling, A. Forster, V. E. Fortov, V. K. Gryaznov, and A. Ya. Polishchuk, *Thermophysical Properties of Hot Dense Plasmas* (Teubner Verlagsgesellschaft, Stuttgart, 1991).